Science
AAAS

The Shape and Surface Variation of 2 Pallas from the Hubble Space Telescope
B. E. Schmidt, *et al.*
Science **326**, 275 (2009);
DOI: 10.1126/science.1177734

Measurements of $\langle I^2_{h/e}\rangle^{1/2}$ for each sample and $\langle I^2_{h/2e}\rangle^{1/2}$ for the smallest rings are shown as a function of T for $\theta = 45°$ (open symbols) and $\theta = 6°$ (solid symbols) (Fig. 3). It can be seen that the PC in larger rings decays more quickly with T than in smaller rings, and that $\langle I^2_{h/2e}\rangle^{1/2}$ decays more quickly than $\langle I^2_{h/e}\rangle^{1/2}$, which is consistent with the discussion above. In addition, the agreement between the data for the r = 418 nm array and the r = 418 nm single ring indicates that the PC signal scales as $\sqrt{N}$ and hence that the PC is random from ring to ring.

The solid lines are fits to theoretical predictions in which $\langle I^2_{h/pe}\rangle^{1/2}$ is calculated for diffusive non-interacting electrons. This calculation closely follows that of (*17*) but takes into account the presence of the large magnetic field B inside the metal (which lifts the spin degeneracy and breaks time-reversal symmetry) as well as spin-orbit scattering (the rings' circumference exceeds the spin-orbit scattering length, as discussed in the SOM text). We find

$$\left\langle I^2_{h/pe}(T)\right\rangle = g\left(p^2\frac{T}{T_{\mathrm{T}}}\right)\left\langle I^2_{h/pe}(0)\right\rangle \qquad (2)$$

where $g(x) = \frac{\pi^6}{3}x^2\sum_{n=1}^{\infty} n\,\exp\left[-(2\pi^3 nx)^{1/2}\right]$, $\langle I^2_{h/pe}(0)\rangle^{1/2} = 0.37p^{-3/2}\frac{3eD}{(2\pi r)^2}$, and $T_{\mathrm{T}} = \frac{h\pi^2 D}{k_{\mathrm{B}}(2\pi r)^2}$.

The data from each sample were fit separately, in each case using D as the only fitting parameter. The best-fit values of D are listed in Table 1. These values are typical for high-purity evaporated Al wires of the dimensions used here (*21*, *22*); however, to further constrain the comparison between our data and theory, we also independently determined D from the resistivity of a co-deposited wire (the wire's properties are listed in Table 1). This measurement is described in detail in the SOM text and provides a value of D in good agreement with the values extracted from the PC measurements. The values of D in Table 1 show a correlation with the samples' linewidths, which may reflect the increased contribution of surface scattering in the narrower samples.

The calculation leading to Eq. 2 assumes the phase-coherent motion of free electrons around the ring. Measurements of the phase coherence length $L_\Phi(T)$ in the co-deposited wire are described in the SOM text and show that $L_\Phi \gg 2\pi r$ for nearly all the temperatures at which the PC is observable. The closest approach between L_Φ and $2\pi r$ at a temperature where the PC can still be observed occurs in the 308-nm array at T = 3 K, where we find $L_\Phi(3\ \mathrm{K}) = 1.86 \times (2\pi r)$. It is conceivable that the more rapid decrease in $\langle I^2_{h/e}\rangle^{1/2}$ observed in this sample above T = 2 K (Fig. 3) is due to dephasing; however, it is not possible to test this hypothesis in the other samples, because the larger rings' PC is well below the noise floor when $L_\Phi(T) = 1.86 \times (2\pi r)$. To the best of our knowledge the effect of dephasing on the PC has not been calculated.

Our measurement of the PC in normal metal rings over a wide range of temperatures, ring sizes, array sizes, magnetic field magnitudes, and magnetic field orientations with high SNR, excellent background rejection, and low measurement back-action indicates that the rings' equilibrium state is well described by the diffusive non-interacting electron model. In addition to providing a clear experimental picture of PCs in simple metallic rings, these results open the possibility of using measurements of the PC to search for ultra–low temperature phase transitions (*6*) or to study a variety of many-body and environmental effects relevant to quantum phase transitions and quantum coherence in solid-state qubits (*23*, *24*). Furthermore, the micromechanical detectors used here are well suited to studying the PC in circuits driven out of equilibrium (for example, by the controlled introduction of microwave radiation) (*8*). The properties of PCs in these regimes have received relatively little attention to date but could offer new insights into the behavior of isolated nanoelectronic systems.

References and Notes

1. M. Buttiker, I. Imry, R. Landauer, *Phys. Lett.* **96A**, 365 (1983).
2. L. Saminadayar, C. Bäuerle, D. Mailly, *Encycl. Nanosci. Nanotech* **3**, 267 (2004).
3. H. Bluhm, N. C. Koschnick, J. A. Bert, M. E. Huber, K. A. Moler, *Phys. Rev. Lett.* **102**, 136802 (2009).
4. V. Ambegaokar, U. Eckern, *Phys. Rev. Lett.* **65**, 381 (1990).
5. V. Ambegaokar, U. Eckern, *Europhys. Lett.* **13**, 733 (1990).
6. H. Bary-Soroker, O. Entin-Wohlman, Y. Imry, *Phys. Rev. Lett.* **101**, 057001 (2008).
7. U. Eckern, P. Schwab, *Adv. Phys.* **44**, 387 (1995).
8. V. E. Kravtsov, V. I. Yudson, *Phys. Rev. Lett.* **70**, 210 (1993).
9. P. Schwab, U. Eckern, *Z. Phys. B* **103**, 97 (1997).
10. A. C. Bleszynski-Jayich, W. E. Shanks, R. Ilic, J. G. E. Harris, *J. Vac. Sci. Technol. B* **26**, 1412 (2008).
11. A. C. Bleszynski-Jayich, W. E. Shanks, J. G. E. Harris, *Appl. Phys. Lett.* **92**, 013123 (2008).
12. E. M. Q. Jariwala, P. Mohanty, M. B. Ketchen, R. A. Webb, *Phys. Rev. Lett.* **86**, 1594 (2001).
13. M. E. Huber *et al.*, *Rev. Sci. Instrum.* **79**, 053704 (2008).
14. D. Mailly, C. Chapelier, A. Benoit, *Phys. Rev. Lett.* **70**, 2020 (1993).
15. W. J. Skocpol *et al.*, *Phys. Rev. Lett.* **56**, 2865 (1986).
16. P. A. Lee, A. D. Stone, H. Fukuyama, *Phys. Rev. B* **35**, 1039 (1987).
17. E. K. Riedel, F. von Oppen, *Phys. Rev. B* **47**, 15449 (1993).
18. L. P. Levy, G. Dolan, J. Dunsmuir, H. Bouchiat, *Phys. Rev. Lett.* **64**, 2074 (1990).
19. B. L. Altshuler, Y. Gefen, Y. Imry, *Phys. Rev. Lett.* **66**, 88 (1991).
20. V. Chandrasekhar *et al.*, *Phys. Rev. Lett.* **67**, 3578 (1991).
21. P. LaFarge, P. Joyez, D. Esteve, C. Urbina, M. H. Devoret, *Nature* **365**, 422 (1993).
22. C. Song *et al.*, *Phys. Rev. B* **79**, 174512 (2009).
23. P. Cedraschi, V. V. Ponomarenko, M. Büttiker, *Phys. Rev. Lett.* **84**, 346 (2000).
24. A. Kopp, K. Le Hur, *Phys. Rev. Lett.* **98**, 220401 (2007).

25. We thank M. Devoret, R. Ilic, T. Ojanen, and J. C. Sankey for their assistance. A.C.B.-J., W.E.S., and J.G.E.H. are supported by NSF grants 0706380 and 0653377. F.v.O. is supported in part by the Deutsche-Israelische Projektkooperation. J.G.E.H. acknowledges support from the Sloan Foundation. A.C.B.-J. acknowledges support from UNESCO-L'Oreal. L.G. is supported in part by U. S. Department of Energy grant DE-FG02-08ER46482. F.v.O and L.G. acknowledge the hospitality of the Kavli Institute for Theoretical Physics in the final stages of this work.

Supporting Online Material

www.sciencemag.org/cgi/content/full/326/5950/272/DC1
SOM Text
Figs. S1 to S18
References and Notes

23 June 2009; accepted 8 September 2009
10.1126/science.1178139

The Shape and Surface Variation of 2 Pallas from the Hubble Space Telescope

B. E. Schmidt,[1]* P. C. Thomas,[2] J. M. Bauer,[3] J.-Y. Li,[4] L. A. McFadden,[4] M. J. Mutchler,[5] S. C. Radcliffe,[6] A. S. Rivkin,[7] C. T. Russell,[1] J. Wm. Parker,[8] S. A. Stern[8]

We obtained Hubble Space Telescope images of 2 Pallas in September 2007 that reveal distinct color and albedo variations across the surface of this large asteroid. Pallas's shape is an ellipsoid with radii of 291 (±9), 278 (±9), and 250 (±9) kilometers, implying a density of 2400 (±250) kilograms per cubic meter—a value consistent with a body that formed from water-rich material. Our observations are consistent with the presence of an impact feature, 240 (±25) kilometers in diameter, within Pallas's ultraviolet-dark terrain. Our observations imply that Pallas is an intact protoplanet that has undergone impact excavation and probable internal alteration.

In the current paradigm, the largest asteroids were among the first solar system bodies to form and were the building blocks of planets [e.g., (*1*) and references therein]. Pallas is the second largest and third most massive asteroid, with a mean radius of 272 km; 1 Ceres is 475 km (*2*) and 4 Vesta is 265 km (*3*). These three bodies are the archetypes of their spectral classes: Ceres is the largest of the rare G-types, Vesta is the likely parent body of the Vestoid V-type asteroids and the associated howardite, eucrite, and diogenite (HED) meteorites [e.g., (*1*)], and Pallas is the largest of the B-types. Like Vesta, Pallas is linked to an orbital family sharing its orbital and spectral parameters. The largest of these is 5222 Ioffe, with a diameter of 22 km (*4*). It is assumed that

[1]Institute of Geophysics and Planetary Physics, University of California, Los Angeles, CA 90095, USA. [2]Department of Astronomy, Cornell University, Ithaca, NY 14853, USA. [3]Jet Propulsion Laboratory, Pasadena, CA 91109, USA. [4]Department of Astronomy, University of Maryland, College Park, MD 20742, USA. [5]Space Telescope Science Institute (STScI), Baltimore, MD 80302, USA. [6]Hydraulx, Santa Monica, CA 90401, USA. [7]Applied Physics Laboratory, Laurel, MD 20723, USA. [8]Southwest Research Institute, Boulder, CO 80302, USA.

*To whom correspondence should be addressed. E-mail: britneys@ucla.edu

the family formed when one or more large impacts on Pallas ejected pieces of the asteroid into space, but no craters or satellites of Pallas have been reliably detected. Like Ceres, Pallas has a surface covered with hydrated minerals and a semimajor axis near 2.7 AU, consistent with the bodies forming from a common reservoir of water-rich material (*5*, *6*). Pallas differs from Ceres in that it does not appear to have a hydrostatically relaxed shape, yet it is far from irregularly shaped. Ceres and Vesta are best regarded as intact, differentiated "protoplanets," minor bodies whose properties are closer to those of planets than to those of small asteroids [e.g., (*7*)]. Pallas has been less well characterized because until recently no spatially resolved observations existed. In 2007 we observed Pallas near its opposition in five filters with the Wide Field and Planetary Camera 2 (WFPC2) onboard the Hubble Space Telescope (HST), resolving its shape and surface.

We used calibrated WFPC2 images (*8*) to generate a first-order triaxial model for Pallas's shape and size, following a method similar to that of (*9*). The model is based on fits to Pallas's limb with interactive modification to match the nonellipsoidal shape (*8*). Our best fits yielded semiaxes of 291 (±9) km, 278 (±9) km, and 250 (±9) km. We found a rotational pole of RA 42° (±10°), Dec −12° (±10°), within uncertainties of recent measurements (*10*, *11*). We observed Pallas with sub-Earth latitude near 30°S so that the visible surface extended from 60°N through the south pole. The HST solution has a mean radius within 6 km of an occultation-derived shape of 287 (±10) km by 263 (±10) km by 250 (±10) km (*12*), which provides the best check of absolute scale but is up to 19 km larger than other estimates (*8*, *10*, *11*, *13*) (table S1). Our shape and the best estimate of Pallas's mass [see (*8*) for discussion], 1.026 (±0.028) × 10^{-10} solar masses (2.04 × 10^{20} kg) (*14*), imply a density of 2400 (±250) kg/m^3. Agreement with occultation data (*12*) indicates that Pallas has a density intermediate between Ceres at 2077 kg/m^3 (*2*) and Vesta at 3480 kg/m^3 (*3*, *14*).

After measuring Pallas's size, we deconvolved the images to enhance the sharpness of the limb and surface features (*8*). To first order, Pallas's shape is a triaxial ellipsoid, but closer examination of the deconvolved images reveals departures from a regular shape (Fig. 1). Because the observations were made at low phase, the shape of the asteroid's limb results from topography. We observed more than 80% of a full rotation with small coverage gaps, during which Pallas's apparent shape varied from oblate to an irregular spheroid to "egg-shaped." Along the southeastern limb of the image at 348°E (Fig. 1) is a large depression that cuts into the body and could have been caused by impact. This feature is face-on in three subsequent images (central longitudes 62°, 74°, and 75°E), corresponding to Pallas's darkest terrain, and is the largest topographic feature we detected. Similarly shaped smaller features are seen on the limbs of the images at 0°E and 62°E.

To visualize the asteroid's shape, we modeled Pallas by fitting a three-dimensional triaxial ellipsoid to individual WFPC2 images with the modeling program Maya (Fig. 2) (*15*). A digital model with Pallas's dimensions and pole was generated, placed over each image, and fit by hand to the limb's shape. The model was then rotated to the next sub-Earth longitude, mimicking Pallas's rotation between the HST exposures, and shaped again. These steps were repeated for each image until a fully three-dimensional, rotating model of Pallas was complete. The result is a model that matches the images and, by interpolating a smooth body between the available data, allows surface topography to be viewed. Combined interpretation of images and the model shows that Pallas is irregular on scales of ~100 km with several depressions at varying sizes. The largest of these features is centered near 30°S, 75°E and measures about 240 ± 25 km in diameter, visible at several geometries (Fig. 3). Pallas's surface gravity is near 0.18 m/s, close to that of Vesta (*3*). Vesta's large south polar crater has a diameter of 460 km with a prominent central peak (*3*). Following the same gravity scaling laws as for Vesta and the Moon (*3*, *16*, *17*), a 240-km crater on Pallas lies near the transition between simple and complex craters. Vesta's large crater has an estimated depth of 13 km, but a crater's depth is dependent on its type. A bowl-shaped simple crater of ~15 km depth and 240 km diameter would eject a volume of ~3.5 × 10^5 km^3, exceeding the ~5575 km^3 maximum volume of Ioffe, the orbital family's largest member other than Pallas. Therefore, a single impact of this size may be sufficient to have created the Pallas family.

Previous studies of Pallas limited its surface albedo variation to 2% (*18*); however, albedo markings are clearly visible in the deconvolved images (Fig. 1). Pallas's average reflectance properties were obtained from photometry before deconvolution by integrating over the entire visible surface (*8*). The shape of a light curve is related to the size of the body by the relationship

$$\log(b/a) \leq \Delta M(-0.4) \quad (1)$$

(*19*), where a and b are the long and intermediate axes, and ΔM is light-curve amplitude. The max-

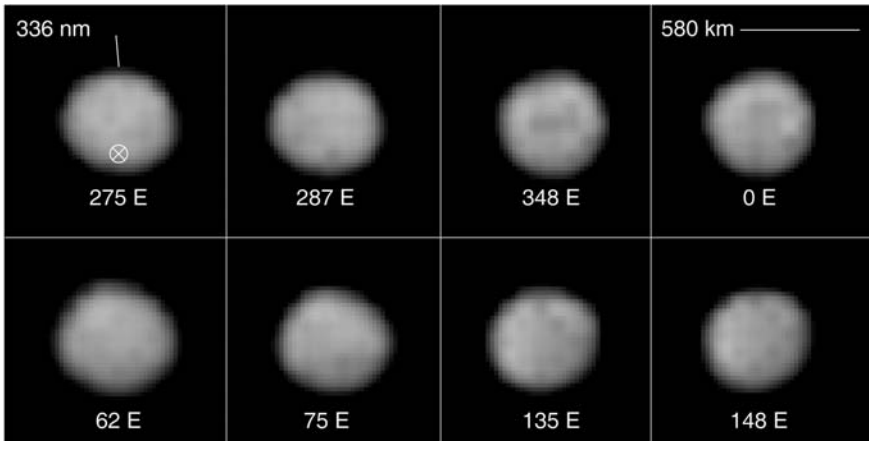

Fig. 1. Deconvolved 336-nm WFPC2 images of Pallas from 8 September 2007. We observed Pallas at an angular size of 0.326 arc sec and a phase of 4.2°, resulting in a scale of ~75 km/pixel. Pallas' spin pole (pointing upward) and south pole (⊗) are marked, and the corresponding sub-Earth longitude is labeled; north is up and east is right in this panel.

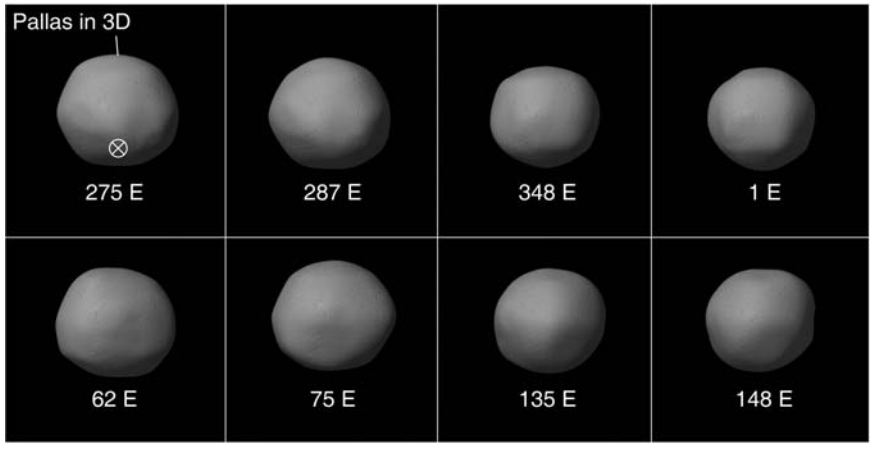

Fig. 2. Three-dimensional topography model of Pallas based on images. The aspects are identical to those in Fig. 1. The approximate orientation of the spin axis and location of the south pole are shown. The texture of the surface is for presentation only.

imum light-curve amplitude in U (*9*) is 0.113 (±0.002) magnitudes, whereas it is 0.091, 0.090, 0.081, and 0.088 (±0.002) magnitudes in the B, V, R, and I filters, respectively (fig. S1). With its *b*/*a* axis ratio of 0.96, this is roughly consistent with the amplitude of the B, V, R, and I light curves deriving from Pallas's shape with a small enhancement due to spatial variation. However, the amplitude in U [near-ultraviolet (UV)] is more than twice that expected from Pallas's shape, suggesting a bright region near 270°E and a dark spot at 70°E. The near-UV wavelength map of Pallas confirms the existence of albedo features, and the locations of the dark and bright terrain agree with those predicted by the light curves (Fig. 4). These terrains correspond to the maxima and minima of the color plot (Fig. 4), confirming that these regions have different colors from each other and from the rest of Pallas's surface. The actual brightness variations across the surface are ~10% above and below the mean. There are also both gradual trends from bright to dark and distinct albedo regions: bright areas near 15°S, 170°E and 45°S, 290°E, and dark regions at 30°S, 0°E and 0°S, 95°E.

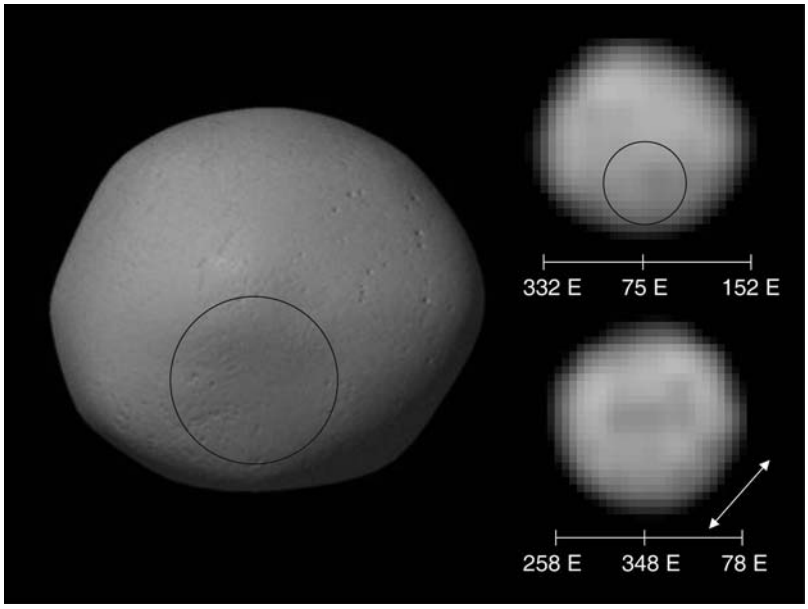

Fig. 3. Pallas's largest crater-like feature seen in the digital model (left) and from two perspectives: appearing face-on (upper right) and edge-on along the limb (lower right). The flat region indicated by the arrow rotates through multiple projections, manifests as the depression in the center of the model, and has a diameter of 240 ± 25 km.

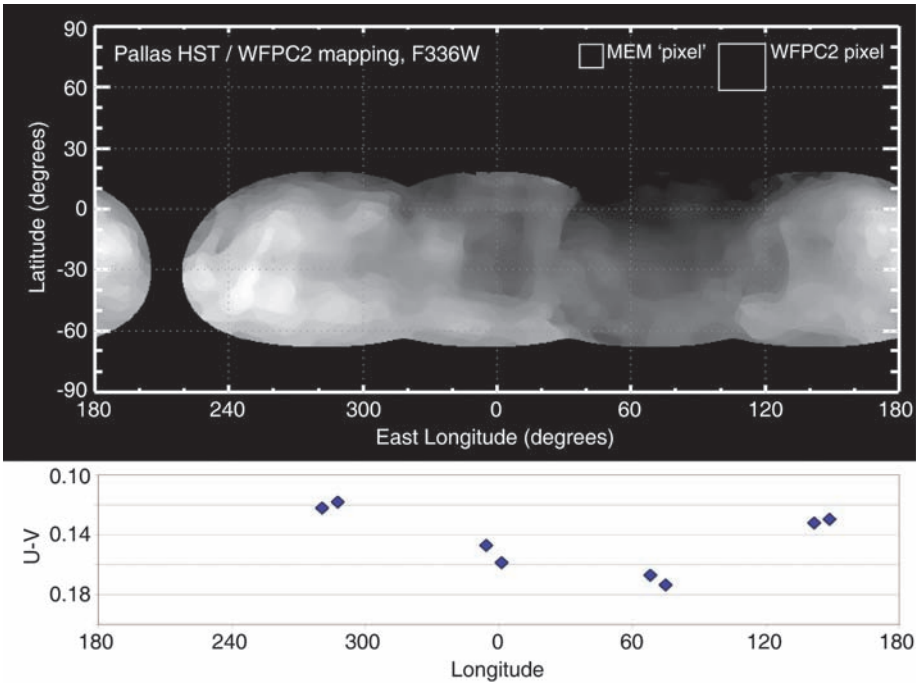

Fig. 4. Map of Pallas in the UV along with its U-V colors constructed from the deconvolved images. The map has been stretched to ± 20% contrast to show variations more clearly. The color plot compares the disk-averaged brightness of the surface in two wavelengths, minimizing shape effects. We show the relative pixel scales of the raw and deconvolved images in the upper right. Any feature smaller than a WFPC2 pixel is beyond our resolution.

Within observational limitations, small, undifferentiated asteroids usually have compositionally homogeneous surfaces, with variations in albedo dominated by regolith effects (*20*, *21*). By contrast, Ceres and Vesta, which are thermally altered bodies, have been shown to possess surface color variation caused by regional differences in processing or composition (*22*, *23*). Both Pallas and Ceres show surface variation that is most pronounced in the near-UV (*22*), and on Ceres, large circular albedo features have been interpreted as craters (*22*, *24*). On Pallas, local topography is on a scale similar to that of albedo features, and the largest potential crater is centered near the UV-dark terrain. Because the albedo trends on Pallas are regionally distinct and wavelength-dependent, the variation is most likely due to a difference in composition or in processing, and not to shadows or regolith effects. Two hypotheses have been presented for altering the UV color of C-type asteroids: space weathering [e.g., (*25*)] and heating (*26*). International Ultraviolet Explorer (IUE) data show that space weathering may brighten the surface in the UV, increasing its spectral slope (*25*), meaning that young surfaces will appear darkest. Additionally, laboratory heating of chondritic material has been shown to increase the material's UV absorption, effectively darkening the material (*26*). The production of darker material could be due to either impact heating or exposure of deeper, more internally heated layers. In either case, impacts are expected to produce UV-dark material, consistent with the interpretation that the UV-dark surfaces on Pallas have undergone impact excavation.

Our measurement of Pallas's shape and surface properties is consistent with a body that has undergone alteration. Because Pallas is too large for significant porosity (*27*), its density implies that Pallas probably formed from a mix of ice, rock, and hydrated silicate. The largest uncertainty in Pallas's interior state arises from uncertainties in its mass (*8*), but its surface materials provide further clues. The hydrated material that covers Pallas has reflective properties similar to those of chondritic material (*28*), and chondrites heated in the lab to temperatures above 400°C have similar UV properties (*26*). If Pallas's surface material is derived from the asteroid and not from meteoritic infall, this suggests that Pallas's surface and interior were thermally altered by impact or internal heat while the body contained a large amount of water. By analogy to evolution scenarios suggested for Ceres (*29*), Pallas contained enough rocky material to undergo

significant internal heating and could differentiate if it formed before the decay of ^{26}Al. Indeed, if Pallas and Ceres did form contemporaneously with similar initial composition, Pallas could retain less heat and water because of its smaller size. Our fit shape is close to that of a hydrostatically relaxed spheroid, which for a mean density of 2400 kg/m^3 would have a and c axes of 283.4 and 251.6 km, respectively, at Pallas's current spin period. These dimensions correspond to the undifferentiated case; our uncertainties would not allow any discrimination of the few-kilometer difference reasonable differentiated models would make. In either case, Pallas's density and spectral properties are suggestive of a body in which water has played a key role. These new measurements of Pallas's size, shape, and reflectance build the case that it joins Ceres and Vesta as the third intact protoplanet: an evolved body with planet-like properties.

References and Notes

1. C. T. Russell *et al.*, *Earth Moon Planets* **101**, 65 (2007).
2. P. C. Thomas *et al.*, *Nature* **437**, 224 (2005).
3. P. C. Thomas *et al.*, *Science* **277**, 1492 (1997).
4. S. Foglia, G. Masi, *Minor Planet Bull.* **31**, 100 (2004).
5. M. A. Feierberg, L. A. Lebofsky, H. P. Larson, *Geochim. Cosmochim. Acta* **14**, 719 (1981).
6. A. S. Rivkin, E. S. Howell, F. Vilas, L. A. Lebofsky, in *Asteroids III*, W. F. Bottke Jr., A. Cellino, P. Paolicchi, R. P. Binzel, Eds. (Univ. of Arizona Press, Tucson, AZ, 2002), pp. 235–253.
7. T. B. McCord, L. A. McFadden, C. T. Russell, C. Sotin, P. C. Thomas, *Eos* **87**, 105 (2006).
8. See supporting material on *Science* Online.
9. P. C. Thomas *et al.*, *Icarus* **135**, 175 (1998).
10. J. D. Drummond, J. Christou, *Icarus* **197**, 480 (2008).
11. B. Carry *et al.*, *Lunar Planet. Inst. Contrib.* **1805**, 8303 (2008).
12. D. W. Dunham *et al.*, *Astron. J.* **99**, 1636 (1990).
13. J. D. Drummond, W. J. Cocke, *Icarus* **78**, 323 (1989).
14. A. S. Konopliv, C. F. Yoder, E. M. Standish, D. N. Yuan, W. L. Sjogren, *Icarus* **182**, 23 (2006).
15. Maya is distributed through the Autodesk EULA agreement.
16. W. Hale, R. A. Grieve, *J. Geophys. Res.* **87**, A65 (1982).
17. H. J. Melosh, *Impact Craters: A Geologic Process* (Oxford Univ. Press, New York, 1989).
18. O. Saint Pe, M. Combes, F. Rigaut, *Icarus* **105**, 263 (1993).
19. K. Meech, J. M. Bauer, O. R. Hainaut, *Astron. Astrophys.* **326**, 1268 (1997).
20. D. B. J. Bussey *et al.*, *Icarus* **155**, 38 (2002).
21. A. Fujiwara *et al.*, *Science* **312**, 1330 (2006).
22. J.-Y. Li *et al.*, *Icarus* **182**, 143 (2006).
23. R. P. Binzel *et al.*, *Icarus* **128**, 95 (1997).
24. B. Carry *et al.*, *Astron. Astrophys.* **478**, 235 (2008).
25. A. R. Hendrix, F. Vilas, *LPI Contrib.* **1805**, 8361 (2008).
26. T. Hiroi, M. E. Zolensky, C. M. Pieters, M. E. Lipschutz, *Meteoritics* **31**, 321 (1996).
27. D. Britt, D. Yeomans, K. Housen, G. Consolmagno, in *Asteroids III*, W. F. Bottke Jr., A. Cellino, P. Paolicchi, R. P. Binzel, Eds. (Univ. of Arizona Press, Tucson, AZ, 2002), pp. 485–500.
28. H. P. Larson, M. A. Feierberg, L. A. Lebofsky, *Icarus* **56**, 398 (1983).
29. T. B. McCord, C. Sotin, *J. Geophys. Res.* **110**, E05009 (2005).

30. Based on observations made with the NASA/ESA Hubble Space Telescope, obtained at the Space Telescope Science Institute, which is operated by the Association of Universities for Research in Astronomy Inc. under NASA contract NAS 5-26555. The observations are associated with program 11115. Supported by STScI grant HST-GO-11115.01 (C.T.R.).

Supporting Online Material

www.sciencemag.org/cgi/content/full/326/5950/275/DC1
Materials and Methods
Tables S1 and S2
Fig. S1
References

15 June 2009; accepted 21 August 2009
10.1126/science.1177734

Evolutionary Development of the Middle Ear in Mesozoic Therian Mammals

Qiang Ji,[1] Zhe-Xi Luo,[2]* Xingliao Zhang,[3] Chong-Xi Yuan,[1] Li Xu[3]

The definitive mammalian middle ear (DMME) is defined by the loss of embryonic Meckel's cartilage and disconnection of the middle ear from the mandible in adults. It is a major feature distinguishing living mammals from nonmammalian vertebrates. We report a Cretaceous trechnotherian mammal with an ossified Meckel's cartilage in the adult, showing that homoplastic evolution of the DMME occurred in derived therian mammals, besides the known cases of eutriconodonts. The mandible with ossified Meckel's cartilage appears to be paedomorphic. Reabsorption of embryonic Meckel's cartilage to disconnect the ear ossicles from the mandible is patterned by a network of genes and signaling pathways. This fossil suggests that developmental heterochrony and gene patterning are major mechanisms in homplastic evolution of the DMME.

Stem therian mammals of the Mesozoic are relatives to modern marsupials and placentals that make up 99% of living mammals today. The marsupial-placental clade, also known as living Theria, is successively nested within the boreosphenidan mammals, the pretribosphenic mammals, and trechnotherians (*1*–*6*). The trechnotherian clade of living therians and spalacotheroids is one of 20 or so Mesozoic mammaliaform clades (*1*, *5*).

Spalacotheroids are a basal group of the trechnotherian clade (*6*–*10*), characterized by the acute triangulation of the molar cusp pattern, a precursor condition to the tribosphenic molars of the common ancestor to marsupials and placentals (*1*–*10*). Spalacotheroids have ancestral skeletal features of living therians (*9*, *10*). Here, we describe an Early Cretaceous spalacotheroid (Figs. 1 and 2) that sheds light on the evolution of the definitive mammalian middle ear (DMME) (*11*). Whether this key mammalian feature had a singular origin or had evolved multiple times is still being debated (*11*–*16*).

Maotherium asiaticus sp. nov. (*17*) shows a diagnostic pattern of main molar cusps arranged in an almost symmetric triangle, thus also known as symmetrodont molars. The postcanines show an increasingly acute (smaller) angle between cusps B′-A-C from the premolar toward the more posterior molars, a gradient in all symmetrodont mammals but most prominently developed in spalacotheroids (*6*–*10*). The upper cusps B′ and C are slightly conical, more closely resembling those of zhangheotheriids than those of other spalacotheroids. A wear facet is developed along the preparacrista (prevallum) between cusp A (paracone) and cusp B′ on M1 and M2, which erupted first in the molar series. However, the facet is not yet developed on the more posterior molars that would erupt later (*6*, *7*, *9*). Thus, the match of upper and lower wear facets occurred after eruption and after substantial occlusal contact of the upper-lower molars. The triangulated shearing surfaces on the molars suggest that *M. asiaticus* was an insectivorous mammal.

M. asiaticus was a generalized terrestrial mammal. It represented a common ecomorphotype and lifestyle among a wide range of ecomorphotypes of Mesozoic mammals (*18*–*21*). *M. asiaticus* is estimated to have a total body length from 150 mm to 155 mm and to weigh between 72 (scaling from its 28.5-mm mandibular length) and 83 g (scaling from skull length of 36.5 mm) [details in (*22*)]. In the hind-foot digit ray III of *M. asiaticus* and *M. sinensis*, the intermediate phalanx is short relative to the proximal phalanx; the proximal and intermediate phalanges are short relative to the metatarsal. Both suggest a terrestrial habit for *Maotherium*. That *M. sinensis* is a terrestrial mammal is also shown by its manual terminal phalanx shape and by phalangeal ratio that can be correlated with the terrestrial ecomorphotypes of extant mammals (*23*). *Zhangheotherium* and *Maotherium* are basal among spalacotheroids, and both had terrestrial habits (*9*, *10*), suggesting that spalacotheroids ancestrally were terrestrial with generalized locomotory function (*9*, *10*, *24*).

M. asiaticus has an ossified Meckel's cartilage. The cartilage has a compressed and tapering anterior limb that is solidly lodged in the

[1]Institute of Geology, Chinese Academy of Geological Sciences, Beijing 100037, China. [2]Carnegie Museum of Natural History, Pittsburgh, PA 15213, USA. [3]Henan Geological Museum, Zhengzhou 450003, China.

*To whom correspondence should be addressed. E-mail: LuoZ@CarnegieMNH.Org